

# Multi-Constellation ARAIM

## Exploiting Satellite Geometry Change

Mathieu Joerger and Boris Pervan,  
*Illinois Institute of Technology, Chicago, IL*

### BIOGRAPHIES

**Dr. Mathieu Joerger** obtained a Master in Mechatronics from the National Institute of Applied Sciences in Strasbourg, France, in 2002, and a M.S. and a Ph.D. in Mechanical and Aerospace Engineering from the Illinois Institute of Technology (IIT), in 2002 and 2009 respectively. He is the 2009 recipient of the Institute of Navigation (ION) Bradford Parkinson award, and the 2014 recipient of the ION Early Achievement Award. He is currently a research assistant professor at IIT, working on multi-sensor integration, on sequential fault-detection for multi-constellation navigation systems, and on relative and differential receiver autonomous integrity monitoring (RAIM) for shipboard landing of military aircraft.

**Dr. Boris Pervan** is a Professor of Mechanical and Aerospace Engineering at IIT, where he conducts research on advanced navigation systems. Prior to joining the faculty at IIT, he was a spacecraft mission analyst at Hughes Aircraft Company (now Boeing) and a postdoctoral research associate at Stanford University. Prof. Pervan received his B.S. from the University of Notre Dame, M.S. from the California Institute of Technology, and Ph.D. from Stanford University. He is an Associate Fellow of the AIAA, a Fellow of the Institute of Navigation (ION), and Editor-in-Chief of the ION journal NAVIGATION. He was the recipient of the IIT Sigma Xi Excellence in University Research Award (2011, 2002), Ralph Barnett Mechanical and Aerospace Dept. Outstanding Teaching Award (2009, 2002), Mechanical and Aerospace Dept. Excellence in Research Award (2007), University Excellence in Teaching Award (2005), IEEE Aerospace and Electronic Systems Society M. Barry Carlton Award (1999), RTCA William E. Jackson Award (1996), Guggenheim Fellowship (Caltech 1987), and Albert J. Zahm Prize in Aeronautics (Notre Dame 1986).

### ABSTRACT

In this work, a new time-sequential positioning and fault detection method is derived and analyzed for dual-frequency, multi-constellation Advanced Receiver Autonomous Integrity Monitoring (ARAIM). Unlike conventional ‘snapshot’ ARAIM, the time-sequential

approach exploits changes in satellite geometry at the cost of higher computation and memory loads. From the perspective of a user on earth, GNSS satellite motion is small over less-than-ten-minute-long time intervals. But, the *accumulated* geometry variations of redundant satellites from multiple GNSS can be substantial. This paper quantifies the potential performance benefit brought by satellite motion to ARAIM. The first research challenge is to define raw GNSS code and carrier error models, which must account for measurement error correlation over time. These models must also be consistent with currently established ARAIM assumptions on carrier-smoothed code. The second step is to use these raw measurements in estimators and fault-detectors capable of exploiting geometric diversity for positioning, float carrier phase cycle ambiguity estimation, and integrity risk evaluation. In this example implementation, signals from multiple GNSS are arranged in a finite-interval batch-type estimator, and sequentially processed in a sliding window mechanism. We derive a compact, computationally-efficient carrier-smoothed-code-based batch implementation. Fault detection is carried out using a multiple hypothesis batch-solution separation algorithm. Availability is analyzed worldwide for aircraft precision approach navigation applications. Results show dramatic performance improvements for batch ARAIM over snapshot ARAIM, not only to achieve ‘localizer precision vertical’ (LPV) requirements using depleted GPS and Galileo constellations, but also to fulfill much more stringent requirements including a ten meter vertical alert limit.

### INTRODUCTION

This paper describes the design, analysis, and evaluation of a new time-sequential positioning and fault detection method for Advanced Receiver Autonomous Integrity Monitoring (ARAIM) using dual-frequency, multi-constellation Global Navigation Satellite Systems (GNSS). This approach differs from prior work on ‘snapshot’ (or instantaneous) ARAIM algorithms [1-3] in that it exploits the geometric diversity from redundant satellite motion. Geometric diversity provides observability on constant biases [4], and is used in this work to estimate floating (real valued) carrier phase cycle

ambiguities, thereby improving navigation accuracy and integrity.

With the modernization of GPS, the full deployment of GLONASS, and the emergence of Galileo and Beidou, an increased number of redundant ranging signals becomes available, which has recently drawn a renewed interest in RAIM. RAIM exploits redundant measurements to achieve self-contained fault detection at the user receiver [5, 6]. In particular, RAIM can help alleviate requirements on ground monitors. For example, researchers in the European Union and in the United States are investigating ARAIM for worldwide vertical guidance of aircraft [1-3].

One of the primary tasks in RAIM is to evaluate integrity risk, or equivalently, the protection levels (which are probabilistic bounds on positioning errors). Integrity risk is the probability of undetected faults causing unacceptably large positioning errors. Multiple research efforts have recently been conducted to design optimal estimators and detectors that minimize the integrity risk in ARAIM, while meeting specified continuity and accuracy criteria [7-10]. These methods have been employed in the 'ARAIM Milestone 2 Report' (reference [2]) to identify the circumstances under which dual-frequency GPS/Galileo could satisfy LPV-200 requirements globally. The 'localizer precision vertical' (LPV) requirements are set to support vertical navigation during approach operations down to 200-foot altitude above ground. Reference [2] shows that worldwide coverage of LPV-200 is achievable using optimal 'snapshot' ARAIM algorithms for a wide range of nominal measurement error and fault parameters.

However, reference [2] also points out cases where LPV200 is not achieved, for example, when nominal constellations are depleted (i.e., one satellite per constellation being removed or set unhealthy). In addition, the alert limit (i.e., the limit on the acceptable positioning error, which defines hazardous situations) is 35 meters for LPV-200, which is much larger than, for example, the Category II precision approach alert limit requirement of 10 meters [11]. Thus, given that the methods used in [7-10] reach the best achievable performance, and unless additional satellites from GLONASS or Beidou are incorporated, 'snapshot' ARAIM algorithms cannot provide better than global LPV-200 service.

In response, this work explores the potential benefit of new integrity monitoring methods that exploit satellite motion to ARAIM applications using dual-frequency multi-constellation GNSS.

Unlike 'snapshot' ARAIM algorithms, where carrier-smoothed code (CSC) measurements from multiple

satellites are combined at one instant in time, position estimates obtained, for example, from a batch estimator (or finite-interval estimator [12]) are directly derived from time-sequences of raw measurements. The batch is more computation and memory expensive, but it gives the means to exploit the geometric diversity provided by satellite motion over short, five-to-ten-minute-long time intervals.

In the next section of this paper, previous research efforts are outlined, which specifically use geometric diversity for carrier phase-based positioning. These prior references have in common that they rely on large changes in geometry from few ranging sources. Conversely, in this paper, we exploit the combination of small angular variations from many space vehicles (SV) in multiple GNSS.

The third section of this paper addresses the key challenge of measurement error modeling over time. Statistical error models are derived for raw measurements, that are consistent with assumptions made in ARAIM [1-3]. The ARAIM error models given in [1] provide values of the CSC measurement error standard deviations due to satellite clock and orbit ephemeris, troposphere, multipath and receiver noise. For each of these error sources, the paper builds upon the work in [13] to model the time correlation affecting raw code and carrier data. A preliminary experimental data analysis is carried out to validate the satellite clock and orbit ephemeris error model.

These raw measurement error models are then used to design batch-type estimator and detector. In this implementation, a batch estimator is preferred over a Kalman filter (KF) to avoid running banks of KF when evaluating the integrity risk [14]. The batch-type estimator can run sequentially using a sliding-window, and can be formulated in a computationally-efficient process using raw carrier and CSC measurements taken at few, infrequent sample times within the fixed batch interval. Fault detection is performed using a batch-type multiple hypothesis solution separation (MHSS) algorithm. The batch-MHSS approach is similar to snapshot ARAIM, except that a time-sequence of measurements is processed rather than a single set of CSC data, and that the nominal bias due to signal deformation (specified in [1, 2]) is treated differently.

The fifth section of this paper presents a step-by-step analysis of the algorithm for an example location over 24 hours. The section first shows that the raw measurement error models match the ARAIM assumptions on CSC. It then evaluates and analyzes the impact of the batch interval length, and shows that only few samples within the batch period are needed to exploit satellite motion.

Finally, a performance analysis is carried out for aircraft approach applications using ARAIM with dual-frequency GPS and Galileo satellite measurements. The results quantify the substantial reduction in integrity risk achieved using batch ARAIM as compared to the baseline snapshot ARAIM algorithm. Worldwide availability maps show that, unlike snapshot ARAIM, batch ARAIM meets LPV-200 requirements even using poorly performing constellations (e.g., assuming depleted constellations). Under conditions described in the paper, batch ARAIM can even satisfy much more stringent requirements, including a 10 meter alert limit.

## BACKGROUND ON GEOMETRIC DIVERSITY

This work aims at exploiting changes in satellite geometry to obtain fast and accurate estimates of carrier phase cycle ambiguities [4]. The Integrity Beacon Landing System (IBLS) devised in the early 1990's [15], and experimentally demonstrated in [16, 17], was an explicit implementation of this principle for aircraft precision approach and landing. GPS signal transmitters serving as pseudo-satellites ('pseudolites') placed on the ground along the airplane's trajectory provided additional ranging sources and a large geometry change as the receiver's downward-looking antenna flew over the installation. By 2000, Rabinowitz et al. designed a receiver capable of tracking carrier-phase measurements from GPS and from low earth orbiting (LEO) telecommunication constellation GlobalStar [18]. Using GlobalStar satellites' large range variations, precise cycle ambiguity resolution and positioning was achieved within 5 min. Another example of LEO satellite-augmented GPS was analyzed in 2010 [13], where ranging signals from Iridium satellites were combined with GPS to provide worldwide carrier phase positioning and fault-detection using RAIM.

In each of the above references, geometric diversity was provided by the fast relative angular motion between user receiver and the few ranging sources (LEO SV or pseudolites) in view during the five-to-ten minute long mission duration. Conversely, in this work, we only consider measurements from medium earth orbiting (MEO) GNSS satellites, which are slowly moving from the perspective of a user near the surface of the earth. It is the *multiplicity* of ranging sources from several GNSS constellations that is exploited here to achieve large accumulated geometric diversity.

To illustrate this point, Fig. 1 (a) shows the angular variation of GPS and Galileo satellites on azimuth-elevation sky plots over a ten min period, for an example location (at Chicago, IL), at an arbitrary start time. While each individual satellite only exhibits small motion over ten minutes, the accumulated motion of many satellites provides the geometric diversity, which a key source of

observability for carrier phase cycle ambiguity estimation [4].

In comparison, Fig. 1 (b) represents the geometry-information used in the conventional 'snapshot' ARAIM algorithm [1-3]. In 'snapshot' ARAIM, GPS and Galileo raw code measurements are first individually smoothed one-by-one using the carrier in a Hatch filter, which is a geometry-free filtering process. CSC data are then combined for snapshot positioning.

Both snapshot and batch estimation are represented in Fig. 2. Let  $n$  be the number of satellites in view, and  $q$  the number of samples, collected from filter initiation at time-epoch 1 to current time  $q$ . For snapshot estimation, raw code measurements  ${}^i\rho_{1,\dots,q}$  for SV  $i$  (as indicated by the left superscript) are smoothed using carrier data  ${}^i\phi_{1,\dots,q}$  sampled at times 1 to  $q$  (right subscripts). The resulting carrier-smoothed code measurements  ${}^i\bar{\rho}_q$  at time  $q$  for  $i = 1, \dots, n$ , are then used, for example, in a weighted least squares estimator [1], to determine the user's position  $\hat{x}_{SNAP}$  at one instant in time. In contrast, the batch estimator directly uses raw code and carrier signals from all SVs at all times to simultaneously estimate user position  $\hat{x}_{BATCH}$  at time  $q$  and floating cycle ambiguities.

The first key challenge in this work is that the ARAIM measurement error models in [1] were only established for CSC code  ${}^i\bar{\rho}_q$ , using large data collection campaigns in [19, 20]. However, evaluating the batch ARAIM performance requires raw measurement error models for  ${}^i\rho_{1,\dots,q}$  and  ${}^i\phi_{1,\dots,q}$ . The next section addresses this problem.

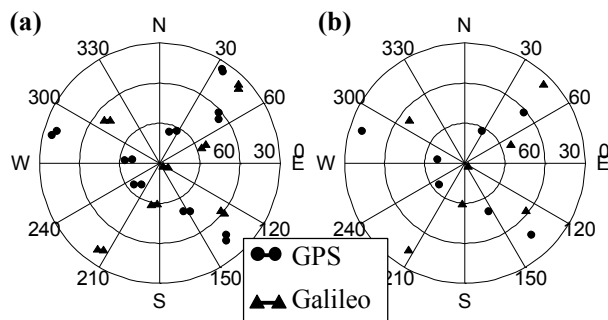


**Fig. 1 Example Azimuth-Elevation Sky Plot**  
**(a) For 'Batch' ARAIM (10 min filtering period)**  
**(b) For 'Snapshot' ARAIM (geometry-free filtering)**

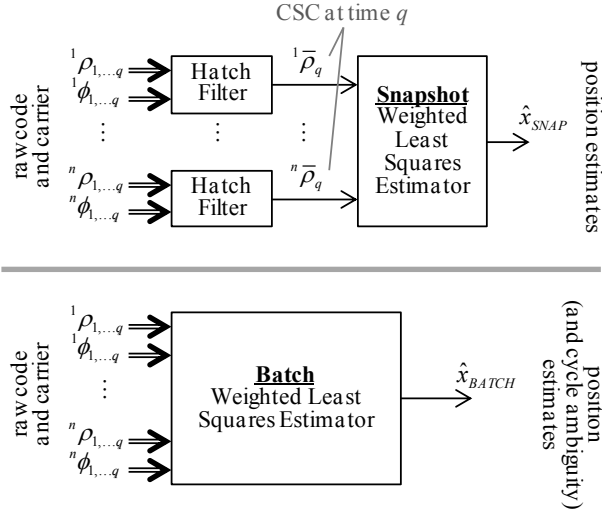


**Fig. 2 Overview of ‘Snapshot’ ARAIM Estimation (top) vs. ‘Batch’ ARAIM (bottom)**

## RAW MEASUREMENT ERROR MODEL DERIVATION

This section aims at deriving statistical error models over time for raw measurements used in batch ARAIM. This work builds upon prior work on measurement error time correlation in [13], and aims at finding error models that are consistent with CSC models experimentally validated in [19, 20], and used in ARAIM [1-3].

The linearized ionospheric-error-free code and carrier phase measurement equations for satellite  $i$  at time  $k$  respectively are:

$${}^i\rho_k = {}^i\mathbf{e}_k^T \mathbf{x}_k + \tau_k + {}^i\varepsilon_{T,k} + {}^i\varepsilon_{E,k} + {}^i\varepsilon_{MP,\rho,k} + {}^i\varepsilon_{RN,\rho,k} + {}^i b_{SD,k} \quad (1)$$

$${}^i\phi_k = {}^i\mathbf{e}_k^T \mathbf{x}_k + \tau_k + {}^i\eta + {}^i\varepsilon_{T,k} + {}^i\varepsilon_{E,k} + {}^i\varepsilon_{MP,\phi,k} + {}^i\varepsilon_{RN,\phi,k} \quad (2)$$

where

- ${}^i\mathbf{e}_k$  is the  $3 \times 1$  line-of-sight vector in a local reference frame (e.g., North-East-Down or NED) for satellite  $i$  at time  $k$
- $\mathbf{x}_k$  is the  $3 \times 1$  user position vector in NED
- $\tau_k$  is the receiver clock offset
- ${}^i\varepsilon_{T,k}$  is the tropospheric error term
- ${}^i\varepsilon_{E,k}$  is the SV clock and orbit ephemeris error
- ${}^i b_{SD,k}$  is a nominal bias due to signal deformation
- ${}^i\eta$  is the carrier phase cycle ambiguity (constant)
- ${}^i\varepsilon_{MP,\rho,k}$  and  ${}^i\varepsilon_{MP,\phi,k}$

respectively are code and carrier multipath errors

$${}^i\varepsilon_{RN,\rho,k} \text{ and } {}^i\varepsilon_{RN,\phi,k}$$

respectively are code and carrier receiver noise terms

The following subsections describe the models assumed for each individual source of error.

## Tropospheric Delay

The tropospheric delay for SV  $i$  at time  $k$  is modeled as:

$${}^i\varepsilon_{T,k} = {}^i c_{T,k} b_{ZTD} + {}^i c_{T,k} \Delta n h_0 (1 - \exp(-h_k / h_0)) \quad (3)$$

where

$b_{ZTD}$  is the zenith tropospheric delay

$\Delta n$  is the tropospheric refractivity error

$h_0$  is the tropospheric scale height

$$(h_0 = 7000\text{m})$$

$h_k$  is the aircraft height at time  $k$

${}^i c_{T,k}$  is the tropospheric zenith-to-slant mapping coefficient:

$${}^i c_{T,k} = 1.001 / \sqrt{0.002001 + (\sin({}^i\theta_k))^2}$$

${}^i\theta_k$  is the elevation angle for SV  $i$  at time  $k$

The first term in (3) is the instantaneous error contribution assumed in snapshot ARAIM [1, 2]. A second term is added in (3) to account measurement error variations caused by changes in aircraft altitude. This extra term is the tropospheric error model used in the Local Area Augmentation System (LAAS) [21]. It is also assumed that the zenith tropospheric delay  $b_{ZTD}$  is zero-mean normally distributed with variance  $\sigma_{ZTD}^2$ . We use the notation:  $b_{ZTD} \sim N(0, \sigma_{ZTD}^2)$  and we assume:  $\sigma_{ZTD} = 0.12$  m [1]. Also, we assume  $\Delta n \sim N(0, \sigma_{\Delta n}^2)$ , with  $\sigma_{\Delta n} = 30$  mm/km.

## Satellite clock and orbit ephemeris error

The satellite clock and orbit ephemeris error equation for satellite  $i$  at time  $k$  is:

$${}^i\varepsilon_{E,k} = {}^i b_E + {}^i g_E(t_k - t_0) + {}^i\varepsilon_{RES,k} \quad (4)$$

where

${}^i b_E$  is an unknown, constant bias

- ${}^i g_E$  is an unknown, constant gradient
- $t_1$  is the first time-epoch of the batch interval
- $t_k$  represents any time  $k$  during the batch interval, such that  $1 \leq k \leq q$ , where  $q$  is the last epoch of the batch interval)
- ${}^i \varepsilon_{RES,k}$  residual errors not captured by bias + ramp

The first term in (4) captures the instantaneous uncertainty in  ${}^i \varepsilon_{E,k}$ . It is therefore set according to ARAIM assumptions as:  ${}^i b_E \sim N(0, \sigma_{URA}^2)$ , where nominally,  $\sigma_{URA} = 1$  m [2].

It can easily be shown that a time-invariant bias  ${}^i b_E$  affecting a sequence of data in Hatch filter causes an error  ${}^i b_E$  to the resulting CSC  ${}^i \bar{\rho}_q$ . But, the ARAIM error model does not specify whether nominal SV clock and orbit errors can be assumed constant. In response, the second term in (4) is added, which is a ramp over time with an unknown but constant gradient  ${}^i g_E$ , accounting for linear variations from the initial value over  $(t_k - t_1)$ . Reference [13] cites references [22-24] to make the following assumption:  ${}^i g_E \sim N(0, (4.7 \cdot 10^{-4} \text{ m/s})^2)$ . Also, reference [13] gives evidence that periodic variations of orbit errors are proportional to the MEO GNSS orbital period, which is much larger than 10 minutes. This supports the linear model assumption.

To further validate equation (4), a preliminary experimental data analysis is carried out. Similar to prior work in [2, 23, 25], precise GPS satellite orbit and clock estimates from the National Geospatial-Intelligence Agency (NGA) are considered ‘truth’ reference data, and are compared to broadcast ephemeris obtained from the Crustal Dynamics Data Information System (CDDIS). However, in contrast with [2, 23, 25], the focus is on the validation of error model characteristics *over time*.

In this preliminary analysis, a limited set of data from June 7, 2015 to June 20, 2015 is processed, for Block IIF satellites including PRNs 1, 3, 6, 9, 26, 27, and 30. The bias-plus-ramp model in equation (4) is fit to truth-minus-broadcast data. Because NGA orbit data is only provided every five minutes, the fit interval is selected to be 30-minute long. This is larger than the example 10-minute batch period assumed in the next sections of this paper, but it will provide conservative results because residual fitting errors are larger over 30 min than they would be over 10 min.

Parameter distributions for  ${}^i b_E$  and  ${}^i g_E$  were established and bounded in the cumulative distribution function

(CDF)-sense [26, 27]. The standard deviations of the over-bounding Gaussian functions are provided in Table 1 for the clock error contribution, and for the three-dimensional orbit errors. Orbit errors are expressed in a local-level, satellite-fixed reference frame, in terms of the in-track, cross-track and radial components [22]. Because GPS satellites are at altitudes of about 20,000 km, user receivers near the surface of the earth are affected by ranging errors that are mostly due to the radial orbit and clock components. Fortunately, radial and clock errors are significantly smaller than in-track and cross-track components, as shown in Table 1.

To get a conservative estimate of the error parameter variance  $\sigma_{BE}^2$  for  ${}^i b_E$  while taking into account the worst-case geometry between SV and user receiver near earth surface, we consider the following equation:

$$\sigma_{BE}^2 = \sigma_{BE,CLK}^2 + \sigma_{BE,R}^2 + 0.24^2 (\sigma_{BE,I}^2 + \sigma_{BE,C}^2) \quad (5)$$

where 0.24 is a multiplier accounting for the worst-case projection of non-radial orbit error components [25], and  $\sigma_{BE,CLK}^2$ ,  $\sigma_{BE,R}^2$ ,  $\sigma_{BE,I}^2$  and  $\sigma_{BE,C}^2$  respectively are the variances of the clock, orbit radial, in-track and cross-track error components contributing to  ${}^i b_E$ . The same can be done for the variance  $\sigma_{GE}^2$  of  ${}^i g_E$ . It follows that  $\sigma_{BE} = 0.65$  m and  $\sigma_{GE} = 1.2 \cdot 10^{-4}$  m/s, which are both smaller than the assumptions made in the upcoming availability analysis (we will assume:  $\sigma_{BE} = 1$  m and  $\sigma_{GE} = 4.7 \cdot 10^{-4}$  m/s). A larger set of data will be analyzed in future work to further validate these numbers.

In addition, the distributions of residual errors  ${}^i \varepsilon_{RES,k}$  are plotted for the clock and radial orbit components in Fig. 3 and 4, respectively.  ${}^i \varepsilon_{RES,k}$  is obtained by removing the best fit bias-plus-ramp model from the truth-minus-broadcast data. The figures show that  ${}^i \varepsilon_{RES,k}$  is not negligible as compared to other error sources affecting carrier measurements. Since we do not know whether these residual errors are due to errors in the NGA ‘truth’ data, we will account for them in the availability analysis, assuming:

$${}^i \varepsilon_{RES,k} \sim N(0, (0.025 \text{ m})^2) \quad (6)$$

where the standard deviation of 0.025 m was obtained using the same formula as in equation (5) but applied to  ${}^i \varepsilon_{RES,k}$  using the bounding standard deviations in the rightmost column of Table 1. Future work will include a detailed analysis of the time-characteristics of  ${}^i \varepsilon_{RES,k}$  which, for now, is modeled as white noise.

**Table 1. Error Model Parameter Over-Bounding Standard Deviations**

	Standard deviation of bounding Gaussian function		
	$b_E$	$g_E$	$\epsilon_{RES}$
Clock	0.47 m	$2.9 \cdot 10^{-5}$ m/s	0.012 m
Orbit radial	0.19 m	$7.5 \cdot 10^{-5}$ m/s	0.02 m
Orbit in-track	1.42 m	$3.2 \cdot 10^{-4}$ m/s	0.018 m
Orbit cross-track	0.96 m	$1.6 \cdot 10^{-4}$ m/s	0.034 m

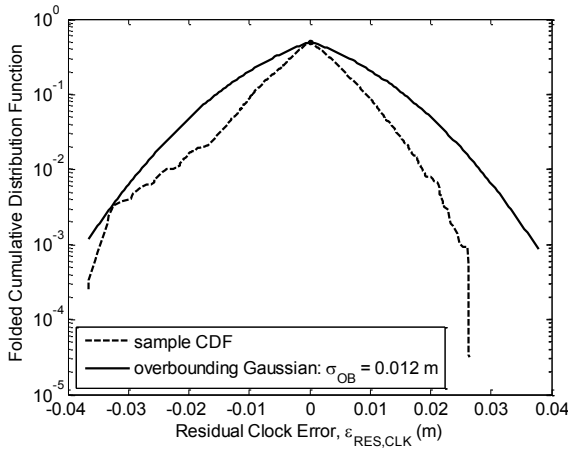


**Fig. 3 Folded CDF (Empirical and Bounding Gaussian) for the SV Clock Error Component of the Best-Fit Bias-Plus-Ramp Model**

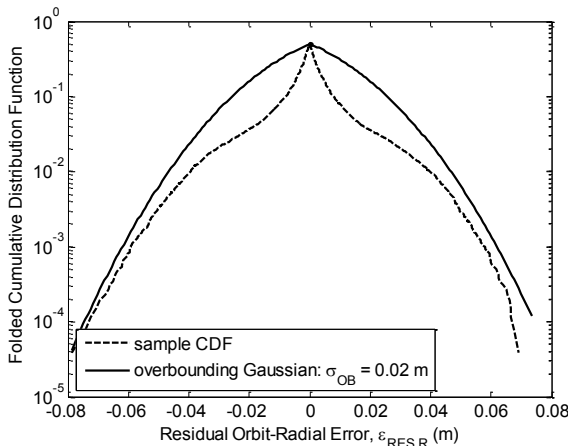


**Fig. 4 Folded CDF (Empirical and Bounding Gaussian) for the Orbit-Radial Error Component of the Best-Fit Bias-Plus-Ramp Model**

## Multipath Error

In this work, time-correlated raw code and carrier measurement errors due to multipath reflections are modeled as first order Gauss Markov Processes (GMP) with time constant  $T_{MP}$ . Using this model, reference [28] provides an expression of the steady-state CSC multipath error variance  ${}^i\sigma_{MP,\bar{p}}^2$  in terms of  $T_{MP}$ , of the Hatch filter (HF) smoothing time  $T_{HF}$ , of the HF sampling interval  $T_S$ , and of raw code and carrier error variances  $\sigma_{MP,\rho}^2$  and  $\sigma_{MP,\phi}^2$ , respectively.  ${}^i\sigma_{MP,\bar{p}}^2$  is given by:

$${}^i\sigma_{MP,\bar{p}}^2 = \frac{\alpha + \alpha\beta - \beta}{(2\alpha - 1)(\alpha - \alpha\beta + \beta)} {}^i\sigma_{MP,\rho}^2 + \frac{2(\alpha - 1)^2(1 - \beta)}{(2\alpha - 1)(\alpha - \alpha\beta + \beta)} {}^i\sigma_{MP,\phi}^2 \quad (7)$$

where  $\alpha = T_{HF}/T_S$  and  $\beta = \exp(-T_S/T_{MP})$

In parallel, ARAIM uses an elevation-dependent model for  $\sigma_{MP,\bar{p}}^2$  [1]. For example, for GPS, the following equation is given:

$${}^i\sigma_{MP,\bar{p},k} = c_{IF} (0.13 + 0.53 \exp(-{}^i\theta_k/10)) \quad (8)$$

where

$c_{IF}$  is the ionosphere-free measurement combination multiplier:

$$c_{IF} = \sqrt{(f_{L1}^4 + f_{L5}^4)/(f_{L1}^2 - f_{L5}^2)^2}$$

$f_{L1}$ ,  $f_{L5}$  respectively are L1 and L5 frequencies

${}^i\theta_k$  is the elevation angle in degrees for SV  $i$  at time  $k$

(A similar model is given in [1] for Galileo.) Equation (8) was established using experimental data collected and analyzed in [19], using  $T_{HF}=100$  s and  $T_S=0.5$  s. And, we assume, based on experimental data analysis in [13, 26], that  ${}^i\sigma_{MP,\phi}^2$  is 100 times smaller than  ${}^i\sigma_{MP,\rho}^2$ . Equation (7) still contains two unknowns:  ${}^i\sigma_{MP,\rho}^2$  and  $T_{MP}$ .

Fortunately, a second set of experimental data was analyzed in [20], which provides a different value of the CSC standard deviation  ${}^i\sigma_{MP,\bar{p},q_{-30s}}$  assuming  $T_{HF}=30$  s. This second relationship provides the means to solve for both unknowns in equation (7). It follows that:

$${}^i\sigma_{MP,\rho,k} = 1.5 {}^i\sigma_{MP,\bar{p},k} \quad , \quad {}^i\sigma_{MP,\phi,k} = 0.015 {}^i\sigma_{MP,\bar{p},k} \quad (9)$$

and  $T_{MP} = 80$  s (10)

### Receiver Noise

The CSC receiver noise standard deviation assumed in ARAIM [1] is given by:

$${}^i\sigma_{RN,\bar{\rho},k} = c_{IF} \left( 0.15 + 0.43 \exp(-{}^i\theta_k / 6.9) \right) \quad (11)$$

Receiver noise is time-uncorrelated. We follow the same approach as for multipath errors in equations (7) to (9), which is simplified because  $T_{MP}$  no longer needs to be determined, and  $\beta = 0$ . Raw code and carrier standard deviations are thus expressed as:

$${}^i\sigma_{RN,\rho,k} = 19.6 {}^i\sigma_{RN,\bar{\rho},k}, \quad {}^i\sigma_{RN,\phi,k} = 0.196 {}^i\sigma_{RN,\bar{\rho},k} \quad (12)$$

Throughout this section, we made the assumption that the error models are robust and accurate over the entire 10-minute-long batch interval. References are cited in [13] to support this assumption, but further experimental validation will have to be carried out in future work. The only source of error left unaddressed in equations (1) and (2) is  ${}^i b_{SD,k}$ , which is dealt with in the next section.

### BATCH ESTIMATOR AND DETECTOR DESIGN

In this section, the measurement error models derived above are incorporated in a batch estimator and in a batch-MHSS RAIM fault-detection algorithm that enables integrity risk evaluation.

#### Batch Measurement Equation

For each SV  $i$ , code and carrier measurements from times 1 to  $q$  are respectively stacked in  $q \times 1$  vectors  ${}^i \boldsymbol{\rho}$  and  ${}^i \boldsymbol{\phi}$ . These vector are then arranged in a  $2qn \times 1$  batch measurement vector:

$$\begin{bmatrix} \boldsymbol{\phi}^T & \boldsymbol{\rho}^T \end{bmatrix}^T = \begin{bmatrix} {}^1\boldsymbol{\phi}^T & \dots & {}^n\boldsymbol{\phi}^T & {}^1\boldsymbol{\rho}^T & \dots & {}^n\boldsymbol{\rho}^T \end{bmatrix}^T \quad (13)$$

This vector can be then expressed in terms of state variables, and of measurement error vectors as:

$$\begin{bmatrix} \boldsymbol{\phi} \\ \boldsymbol{\rho} \end{bmatrix} = \begin{bmatrix} \mathbf{G} & \mathbf{H}_N & \mathbf{H}_{ERR} \\ \mathbf{G} & \mathbf{0}_{qn \times n} & \mathbf{H}_{ERR} \end{bmatrix} \begin{bmatrix} \mathbf{u} \\ \boldsymbol{\eta} \\ \mathbf{s}_{ERR} \end{bmatrix} + \begin{bmatrix} \mathbf{v}_{RNM,\phi} \\ \mathbf{v}_{RNM,\rho} \end{bmatrix} + \begin{bmatrix} \mathbf{0}_{qn \times 1} \\ \mathbf{b}_{SD} \end{bmatrix} \quad (14)$$

where

- $\mathbf{u}$  is a  $5q \times 1$  vector of positions and GPS and Galileo receiver clock offsets at all times
- $\boldsymbol{\eta}$  is an  $n \times 1$  vector of cycle ambiguities:
- $\mathbf{s}_{ERR}$  is a  $2(n+1) \times 1$  vector of constant error states.
- $\mathbf{0}_{a \times b}$  is an  $a \times b$  matrix of zeros

Vector  $\mathbf{u}$  is constructed using the following equations:

$$\mathbf{u} = \begin{bmatrix} \mathbf{u}_1^T & \dots & \mathbf{u}_k^T \end{bmatrix}^T, \quad \mathbf{u}_k = \begin{bmatrix} \mathbf{x}_k^T & \tau_{GPS,k} & \tau_{GAL,k} \end{bmatrix}^T \quad (15)$$

where  $\tau_{GPS,k}$  and  $\tau_{GAL,k}$  are the receiver clock offsets for GPS and Galileo respectively, assuming that the time-offset between the two constellations is unknown.

The vector of constant cycle ambiguities is defined as:

$$\boldsymbol{\eta} = \begin{bmatrix} {}^1\eta & \dots & {}^n\eta \end{bmatrix}^T \quad (16)$$

The vector of error states is given by:

$$\mathbf{s}_{ERR} = \begin{bmatrix} b_{ZTD} & \Delta n & \mathbf{b}_E^T & \mathbf{g}_E^T \end{bmatrix}^T \quad (17)$$

where  $\mathbf{b}_E$  and  $\mathbf{g}_E$  are the  $n \times 1$  vectors of constant clock and orbit ephemeris biases and gradients for all  $n$  satellites constructed following the exact same pattern as  $\boldsymbol{\eta}$  in equation (16). Error states  $\mathbf{s}_{ERR}$  are included in the state vector, not because their estimated values are of interest, but because state augmentation is a practical way to incorporate measurement error dynamics.

The batch geometry matrix  $\mathbf{G}$  and states coefficient matrices  $\mathbf{H}_N$  and  $\mathbf{H}_{ERR}$  are not explicitly expressed here to limit the length of the paper. But a similar batch realization incorporating code and carrier measurements as well as similar error states can be found in [13, 29].

Vector  $[\mathbf{v}_{RNM,\phi}^T \quad \mathbf{v}_{RNM,\rho}^T]$  accounts for receiver noise and multipath affecting carrier phase and code signals. Its covariance matrix is noted  $\mathbf{V}$ . Matrix  $\mathbf{V}$  is block diagonal. Each block for carrier and code corresponds to a satellite. Within each block, off-diagonal components capture the time-correlation due to multipath error, which is modeled as a first order GMP. A more detailed description of how to construct  $\mathbf{V}$  is given in [13, 29].

The  $qn \times 1$  vector of nominal biases due to signal deformation  $\mathbf{b}_{SD}$  for all SVs at all times is arranged the same way  $\boldsymbol{\rho}$  is in equation (13).

The batch measurement equation (14), to which we add a  $2qn \times 1$  batch fault vector  $\mathbf{f}$ , which will have to be detected, can be rewritten in a standard form as:

$$\mathbf{z} = \mathbf{H}\mathbf{x} + \mathbf{v} + \mathbf{f} \quad (18)$$

where

- $\mathbf{z}$  is the batch measurement vector
  - $\mathbf{H}$  is the batch observation matrix,
  - $\mathbf{x}$  is the batch state vector
  - $\mathbf{v}$  is the batch measurement noise vector:
- $$\mathbf{v} \sim N([\mathbf{0}_{qn \times 1}^T \quad \mathbf{b}_{SD}^T]^T, \mathbf{V})$$

### Batch Estimator Design

The batch weighted least-squares (WLS) estimate for the state of interest (e.g., for the vertical position coordinate, which is of primary interest in aircraft approach navigation) obtained using all available measurements is also referred to as full-set solution. It is defined as:

$$\hat{x}_0 \equiv \mathbf{s}_0^T \mathbf{z} \quad (19)$$

where  $\mathbf{s}_0$  is the  $2qn \times 1$  vector of batch WLS coefficients (the same notations, with additional details, are used in [30]). The full-set estimate error is noted  $\varepsilon_0$ :  $\varepsilon_0 \equiv x - \hat{x}_0$ , where  $x$  is the true value of the state of interest.  $\varepsilon_0$  is such that:

$$\varepsilon_0 \sim N(b_0 + \mathbf{s}_0^T \mathbf{f}, \sigma_0^2 \equiv \mathbf{s}_0^T \mathbf{V} \mathbf{s}_0) \quad (20)$$

where  $b_0$  is the impact on state estimation of nominal errors due to signal deformation (SD)  $\mathbf{b}_{SD}$ . The ARAIM error model in [1-2] does not specify whether SD biases  $\mathbf{b}_{SD}$  are constant over time, but it assumes that the elements of  $\mathbf{b}_{SD}$  can all be bounded by a maximum value noted  $b_{nom}$ :  $b_{nom} = 0.75$  m in [2]. We further assume that ranging errors due to SD are different for all satellites, but do not change sign (positive to negative or vice-versa) during the batch time-interval. It follows that  $b_0$  can be bounded by:

$$b_0 \leq |\mathbf{s}_0^T \mathbf{A}| \mathbf{1}_{n \times 1} b_{nom} \quad (21)$$

where  $|\cdot|$  is the element-wise absolute value operator, and:

$$\mathbf{A} = [\mathbf{0}_{qn \times n}^T \quad \mathbf{A}_\rho^T]^T, \quad \mathbf{A}_\rho = \begin{bmatrix} \mathbf{1}_{q \times 1} & \mathbf{0}_{q \times 1} & \cdots & \mathbf{0}_{q \times 1} \\ \mathbf{0}_{q \times 1} & \mathbf{1}_{q \times 1} & & \vdots \\ \vdots & & \ddots & \\ \mathbf{0}_{q \times 1} & \cdots & & \mathbf{1}_{q \times 1} \end{bmatrix}$$

where

$\mathbf{1}_{a \times b}$  is an  $a \times b$  matrix of ones.

### Batch Detector Design

A multiple-hypothesis solution separation (MHSS) batch RAIM method [1, 2, 14, 30, 31] is adopted for detection of  $\mathbf{f}$ . Let  $h$  be the number of fault hypotheses that need to be monitored against (refer to [30] for details on how to determine  $h$ ). A set of mutually exclusive, exhaustive hypotheses  $H_i$ , for  $i=0, \dots, h$ , is considered. Under  $H_i$ , a number  $n_i$  of measurements is simultaneously impacted by the fault. The fault-free subset solution, which excludes these  $n_i$  measurements, is written as:  $\hat{x}_i \equiv \mathbf{s}_i^T \mathbf{z}$ , where  $\mathbf{s}_i$  is the  $2qn \times 1$  vector of the subset solution's batch WLS coefficients with zeros for elements corresponding to the  $n_i$  faulted measurements [30]. Under  $H_i$ , the estimation error  $\varepsilon_i$  of  $\hat{x}_i$  is such that:

$$\varepsilon_i \sim N(b_i + \mathbf{s}_i^T \mathbf{f}, \sigma_i^2 \equiv \mathbf{s}_i^T \mathbf{V} \mathbf{s}_i) \quad (22)$$

where

$$b_i \leq |\mathbf{s}_i^T \mathbf{A}| \mathbf{1}_{n \times 1} b_{nom}. \quad (23)$$

The batch MHSS test statistics are then defined as:

$$\Delta_i \equiv \hat{x}_0 - \hat{x}_i = \mathbf{s}_{\Delta i}^T \mathbf{z}, \text{ for } i=1, \dots, h, \quad (24)$$

$\Delta_i$  is normally distributed with variance

$$\sigma_{\Delta i}^2 = \sigma_i^2 - \sigma_0^2 \quad (25)$$

In snapshot ARAIM, hypotheses  $H_i$  are defined by satellites being faulted or not. Let us consider a fixed subset of satellites being faulted. Batch ARAIM opens the possibility for a sub-subset (within the subset of faulted SV data) of measurements over time being fault-free. When determining faults that need to be monitored against in a batch, it is worth asking whether a larger number of measurements being affected over time necessarily causes a higher integrity risk. On the one hand, more faulted measurements may increase the estimation error, but, on the other hand, it may also provide more opportunities for detection.

In this regard, it can first be reminded that the failure mode slope, which is the ratio of the mean of  $\varepsilon_0$  over the mean of  $\Delta_i / \sigma_{\Delta_i}$ , is shown in [30] to be equal to  $\sigma_{\Delta_i}$ . The larger the failure mode slope  $\sigma_{\Delta_i}$ , the larger the integrity risk [30-32]. It follows that the higher the number of faulted measurements, the higher the fault-free subset solution variance  $\sigma_i^2$ , the higher  $\sigma_{\Delta_i}^2$  in equation (25), and therefore the higher the integrity risk. This means that a fault affecting the complete sequence of measurements, from time epochs 1 to  $q$ , can always cause a larger integrity risk than a fault affecting a subset of these measurements. We therefore consider subset of satellites being faulted from time 1 to  $q$ , but we do not need to consider subset measurement-sequences from some intermediary time  $k \geq 1$  to  $q$ .

### Reduced Batch Implementation

In this section, two additional parameters are defined. Let  $T_B$  be the batch period, i.e., the finite interval over which measurements are processed:  $T_B$  determines the amount of change in SV geometry (e.g., we will use  $T_B=10$  min in the next sections of the paper). Also, let  $T_S$  be the sampling interval, i.e., the time between raw samples within the batch (e.g.,  $T_S=0.5$  s). Batch equations (13) to (25) assume that multi-GNSS measurements are processed at regular  $T_S$ -intervals over  $T_B$ . The dimensions of the resulting batch matrices and vectors are therefore very large, and matrix inversions, needed for example to calculate  $\mathbf{s}_0$  in equation (19), are extremely time consuming.

In response, we derive a reduced batch implementation, illustrated in Fig. 5, based on raw carrier phase and CSC measurements taken at few, infrequent sample times during  $T_B$ . This algorithm exploits the same two fundamental estimation principles as the full batch: (a) raw code measurement errors due to multipath and receiver noise are *averaged out*, in this case using CSC obtained from Hatch filters (HF); (b) *redundant satellite motion* is captured using raw carrier phase measurements at few, temporally-separated sample times.

Let  $T_{RBS}$  be the reduced batch sampling interval within the batch period  $T_B$ . Because in this reduced batch process, noise averaging is performed in separate HF's,  $T_{RBS}$  can be selected much larger than the raw measurement sampling period  $T_S$  ( $T_{RBS} \gg T_S$ ).

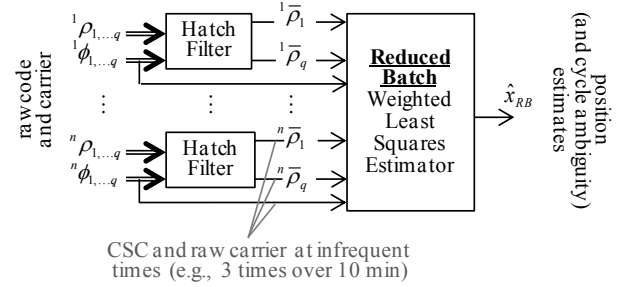


**Fig. 5 Reduced-Batch (RB) ARAIM Implementation**

For example, in the ‘Batch ARAIM Availability Analysis’ Section, we use  $T_B=10$  min, and  $T_{RBS}=5$  min. The resulting number of sample times is reduced from  $q=1200$  for the full batch (for  $T_B=10$  min,  $T_S=0.5$  s) down to  $q=3$  for the reduced batch.

The reduced batch ARAIM MHSS method is the same as the full batch process described in equations (13) to (25), except for two main differences. First, equation (14) becomes:

$$\begin{bmatrix} \boldsymbol{\varphi} \\ \bar{\boldsymbol{\rho}} \end{bmatrix} = \begin{bmatrix} \mathbf{G} & \mathbf{H}_N & \mathbf{H}_{ERR} \\ \mathbf{G} & \mathbf{0}_{qn \times n} & \mathbf{H}_{ERR} \end{bmatrix} \begin{bmatrix} \mathbf{u} \\ \boldsymbol{\eta} \\ \mathbf{s}_{ERR} \end{bmatrix} + \begin{bmatrix} \mathbf{v}_{RNM,\phi} \\ \mathbf{v}_{RNM,\bar{\rho}} \end{bmatrix} + \begin{bmatrix} \mathbf{0}_{qn \times 1} \\ \mathbf{b}_{SD} \end{bmatrix} \quad (26)$$

where

- $q$  is the number of sample times, which is much smaller for the reduced batch than for the full batch
- $\bar{\boldsymbol{\rho}}$  is a  $qn \times 1$  vector of CSC measurements
- $\mathbf{v}_{RNM,\bar{\rho}}$  is a  $qn \times 1$  vector of CSC receiver noise and multipath error terms

Then, the covariance matrix  $\bar{\mathbf{V}}$  of vector  $[\mathbf{v}_{RNM,\phi}^T \ \mathbf{v}_{RNM,\bar{\rho}}^T]$  is no longer block diagonal because raw carrier measurements are correlated with CSC due to Hatch filtering. Complete analytical expressions of the correlation between CSC and raw carrier measurements are given in Appendix. It is worth noting that the 5-minute  $T_{RBS}$ -value used in the next sections of this paper is very large as compared to the multipath correlation time-constant ( $T_{MP}=80$  s) and to the HF smoothing time constant ( $T_{HF}=100$  s). It follows, as explained in Appendix, that the expression of  $\bar{\mathbf{V}}$  can be simply and accurately approximated using blocks of diagonal matrices.

In summary, the reduced batch ARAIM MHSS method presents the following characteristics.

- It is much more computation and memory efficient than the full batch.
- It provides equivalent availability performance to the full batch.
- Since it is based on CSC, it only requires minor modifications of existing snapshot ARAIM algorithms.

The reduced batch implementation in Fig. 5 is used in section ‘Batch ARAIM Availability Analysis’. From now on, it is referred to as ‘batch ARAIM’. The raw-measurement-based batch in equation (14) will be referred to as the ‘full-batch’, and is used in the next section to analyze raw measurement error models.

### Integrity and Continuity Risk Evaluation

The integrity risk, or probability of hazardous misleading information  $P_{HMI}$ , is evaluated using the following upper-bound [30]:

$$P_{HMI} \leq P\left(|\varepsilon_0| > \ell \mid H_0\right)P_{H0} + \sum_{i=1}^h P\left(|\varepsilon_i| + T_i > \ell \mid H_i\right)P_{Hi} \quad (27)$$

where

- $\ell$  is the alert limit (AL) that defines hazardous situations: in [2], the vertical AL is  $\ell=35\text{m}$
- $P_{Hi}$  is the prior probability of  $H_i$  occurrence
- $H_0$  is the fault-free hypothesis
- $H_i$  for  $i=1, \dots, h$  are the fault hypotheses corresponding to faults on subset measurement ‘ $i$ ’ (including single-satellite and multi-satellite faults)

Under fault-free hypothesis  $H_0$ , the detection threshold  $T_i$  is set based on an allocated continuity risk requirement  $C_{REQ}$  (specified in [2]) to limit the probability of false alarms.  $T_i$  can be defined as:

$$T_i = Q^{-1}\left\{C_{REQ}/(2hP_{H0})\right\} \sigma_{\Delta_i} \quad (28)$$

where the function  $Q^{-1}\{\}$  is the inverse tail probability distribution of the two-tailed standard normal distribution.

The following section analyzes the probability distributions of  $\varepsilon_0$ ,  $\varepsilon_i$  and  $\Delta_i$  for batch versus snapshot ARAIM, and for varying values of the batch period.

## ANALYSIS OF MEASUREMENT ERROR MODELS AND OF SNAPSHOT VS. BATCH APPROACHES

This section describes a step-by-step analysis to show that, given  $T_B$  of about 10 minutes, estimation performance improves substantially for batch ARAIM as compared to snapshot ARAIM. The ‘full-batch’ described in equation (14) and based on raw measurements is used in this section.

### ‘Frozen Geometry’ Analysis: Raw Versus CSC Measurement Error Model Comparison

The comparison between snapshot ARAIM and full-batch ARAIM in Fig. 1 and 2 highlights that the main difference between the two approaches is the use of SV motion. Assuming a constant, ‘frozen’ geometry should therefore provide identical performance for both implementations. This point is used to confirm that the raw measurement error models in equations (1) to (12) are consistent with ARAIM CSC models in [1, 2].

To do so, the transient response of the Hatch filter (HF) must also be accounted for, because CSC error models in [1, 2] are specified assuming that the HF has reached steady-state. The steady-state CSC standard deviations are expressed, for example in equation (5) for multipath noise, in terms of  $\alpha = T_{HF}/T_S$ . In parallel, in Appendix A of [29], the variance of the full-batch position estimate assuming a frozen geometry is expressed in terms of the number of samples  $n_S$  ( $n_S = T_B/T_S$ ). These two expressions can be used to determine that equivalent performance is expected when  $T_B = 2T_{HF}$ , i.e., in this case, when  $T_B = 200$  s.

In the following Figures 6 to 8, the means and standard deviations that define the distributions of the random variables of  $P_{HMI}$  in equation (27) are evaluated over 24 hours, at an example Chicago location (25.5 deg N, -80.1 deg E), assuming dual-frequency measurements from GPS and Galileo. Nominal simulation parameters are further described in the next section. The means and standard deviations for full-batch ARAIM are  $\sigma_0$ ,  $b_0$ ,  $\sigma_i$ ,  $b_i$ , and  $\sigma_{\Delta_i}$  defined in equations (20) to (25). The same quantities for snapshot ARAIM are respectively noted  $\underline{\sigma}_0$ ,  $\underline{b}_0$ ,  $\underline{\sigma}_i$ ,  $\underline{b}_i$ , and  $\underline{\sigma}_{\Delta_i}$ . The legend is the same in all three figures.

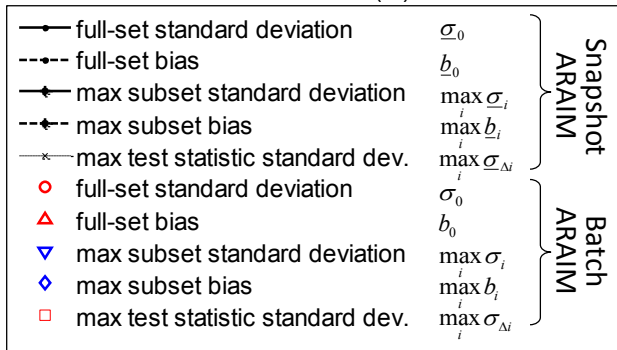
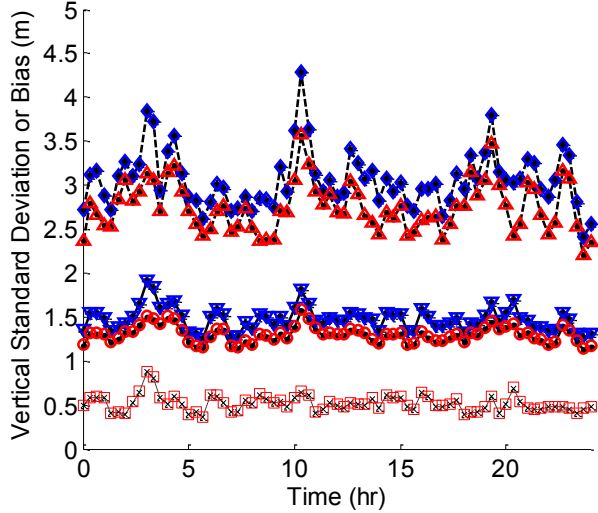


**Fig. 6 Comparing Snapshot and Full-Batch ARAIM to Show that Raw Measurement Error Models are Consistent with ARAIM Assumptions on CSC in [1, 2] (frozen geometry,  $T_B = 200$ s).**

Fig. 6 is established for  $T_B = 200$  s. Snapshot versus full-batch results match closely, which confirms that the raw measurement error models derived earlier are consistent with ARAIM assumptions in [1, 2].

### Impact of Satellite Motion

The estimation error means and standard deviations are plotted in Fig. 7 assuming the same simulation parameters as in Fig. 6, but the geometry is no longer frozen. Fig. 7 shows the substantial impact of satellite motion over  $T_B = 200$  s on estimation performance. It confirms that bias observability using SV motion is a performance-driving principle, together with noise averaging over numerous samples. This effect is further accentuated in Fig. 8, where the batch interval is increased from  $T_B = 200$  s to  $T_B = 600$  s.

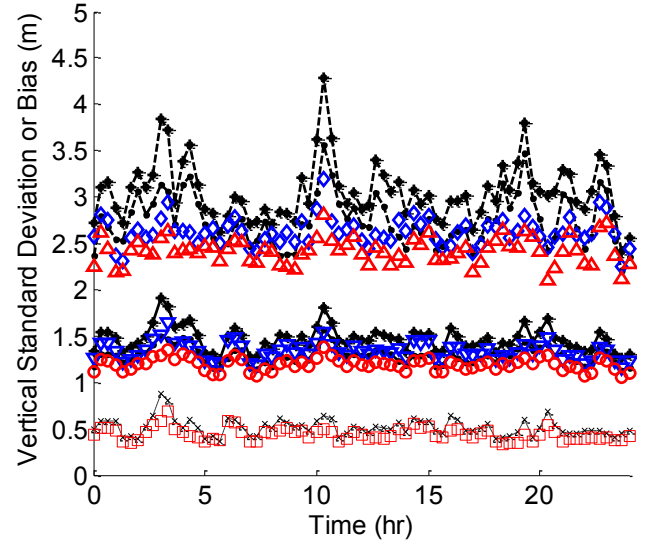


**Fig. 7 Impact of Satellite Motion: all parameters identical to Fig. 6, but geometry is no longer frozen ( $T_B = 200$ s).**

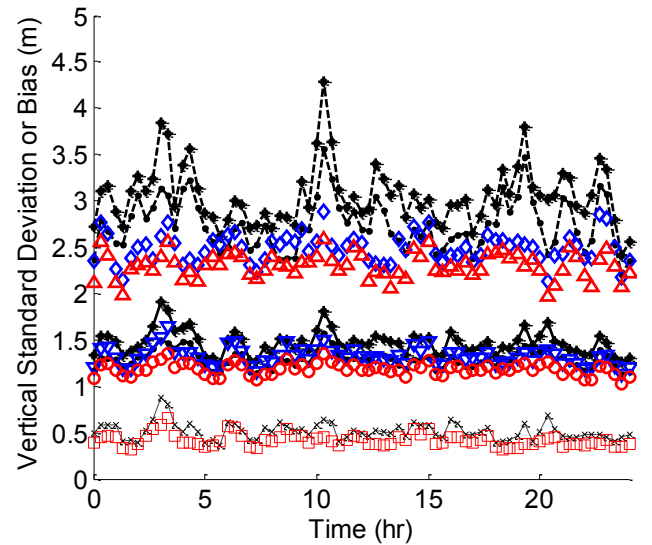


**Fig. 8 Impact of  $T_B$  : all parameters identical to Fig. 7, except  $T_B = 600$ s.**

The integrity risk  $P_{HMI}$  is plotted in Fig. 9 for the full-batch ARAIM ( $T_B = 600$  s,  $T_S = 0.5$  s) and for reduced-batch ARAIM ( $T_B = 600$  s,  $T_{RBS} = 300$  s), over 24 hours, at the example Chicago location. The dashed line in Fig. 7 is the integrity risk requirement  $I_{REQ}$ , specified in [2] to be:  $I_{REQ} = 0.98 \cdot 10^{-7}$  for the vertical position coordinate. Fig. 9 also assumes that the vertical alert limit in equation (24) is  $\ell = 10$  m, that prior probabilities of satellite and constellation faults, noted  $P_{Hi}$  in equation

(24), respectively are  $P_{sat} = 10^{-5}$  and  $P_{const} = 10^{-8}$ , and that the continuity risk requirement in equation (28) is  $C_{REQ} = 3.9 \cdot 10^{-6}$ .

Fig. 9 shows the dramatic  $P_{HMI}$ -reduction obtained using full-batch ARAIM as compared to snapshot ARAIM. In Fig. 9, the fraction of time where the solid curves are below the dashed line is the availability. In this case, availability is 100% for full-batch ARAIM, and is much lower for snapshot ARAIM (65%). In addition, Fig. 9 shows that full-batch ARAIM and reduced-batch ARAIM have overlapping  $P_{HMI}$ -curves, even though reduced-batch ARAIM is much more computation and memory efficient.

### BATCH ARAIM AVAILABILITY ANALYSIS

This section evaluates the global availability of LPV-200 navigation requirements to support localizer precision vertical aircraft approach operations down to 200 feet above the ground, using ARAIM with dual-frequency measurements from GPS and Galileo. Nominal simulation parameters are defined in [2], and include:

- a five degree satellite elevation mask
- ARAIM CSC measurement error model parameters in equations (1) to (10), and (21)
- navigation requirements:  $I_{REQ} = 0.98 \cdot 10^{-7}$ ,  $C_{REQ} = 3.9 \cdot 10^{-6}$ ,  $\ell = 35$  m
- prior probabilities of faults:  $P_{sat} = 10^{-5}$ ,  $P_{const} = 10^{-4}$
- reduced-batch period and sampling interval:  $T_B = 10$  min,  $T_{RBS} = 5$  min
- nominal constellations, comprising 24 GPS satellites and 24 Galileo SVs [33]

These parameters are modified below to evaluate performance sensitivity. In order to account for potential satellite outages, depleted constellations of ‘24-1’ GPS satellites and ‘24-1’ Galileo SVs [33] are considered as well. Additional requirements, including Effective Monitor Threshold (EMT) and fault-free accuracy requirements [2], are included in the simulation but not discussed in this paper as they only have a minor impact on overall availability.

### Batch Vs. Snapshot ARAIM Availability Using Depleted Constellations

Figures 10 and 11 display availability maps for a 10 deg  $\times$  10 deg latitude-longitude grid of locations, for depleted ‘24-1’ GPS and ‘24-1’ Galileo constellations, for satellite geometries simulated at regular 5 minute intervals over a 24 hour period. Availability is computed at each location as the fraction of time where the  $P_{HMI}$ -bound meets  $I_{REQ}$ .

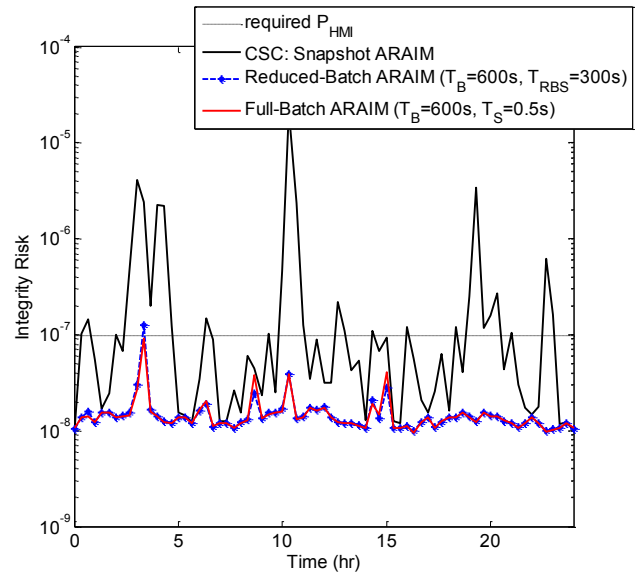


**Fig. 9 Integrity Risk Bound Obtained Using Snapshot Vs. Batch ARAIM: all parameters identical to Fig. 8 ( $T_B = 600s$ ,  $T_{RB} = 300s$ ).**

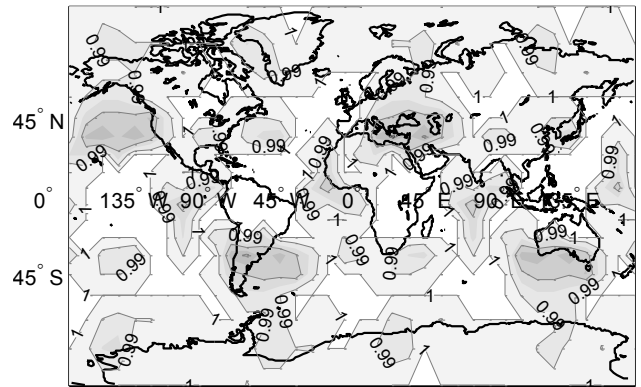


**Fig. 10 Availability Map for Snapshot ARAIM using depleted constellations,  $P_{const} = 10^{-4}$ ,  $\ell = 35$  m (coverage of 99.5% availability is 61%).**

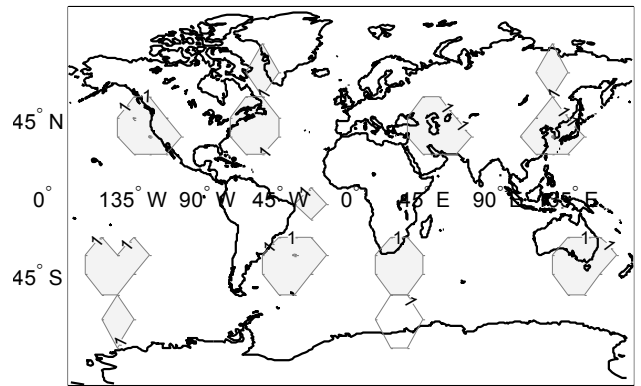


**Fig. 11 Availability Map for Batch ARAIM using depleted constellations,  $P_{const} = 10^{-4}$ ,  $\ell = 35$  m (coverage of 99.5% availability is 99.6%).**

In the figures, availability is color-coded: white color corresponds to a value of 100%, black represents 80%. Constant availability contours are also displayed. The gray areas in Fig. 10 indicate that snapshot ARAIM is clearly outperformed by batch ARAIM in Fig. 11.

The worldwide availability metric given in the figure captions is the weighted coverage of 99.5% availability: coverage is defined as the percentage of grid point locations exceeding 99.5% availability. The coverage computation is weighted at each location by the cosine of the location's latitude, because grid point locations near the equator represent larger areas than near the poles. Fig. 10 and 11 show that the coverage of 99.5% availability increases from 61 % for snapshot ARAIM, to 99.6% for batch ARAIM, assuming  $\ell = 35$  m.

This result was obtained using the 'baseline' snapshot ARAIM algorithm described in [1-3]. Reference [2] also provides an 'optimized' estimator, which, when evaluated under the same assumptions as in Fig. 8, provides coverage of 99.5% availability of 81%. Therefore, even using an optimized estimator, coverage using snapshot ARAIM is 19% lower than using batch ARAIM.

**Batch Vs. Snapshot ARAIM Availability for a Ten Meter Alert Limit**

Figures 12 and 13 evaluate the potential of batch ARAIM to meet requirements that are more stringent than LPV200, including a tight alert limit:  $\ell = 10$  m. One key assumption to achieve high availability is that the prior probability of constellation-wide faults must be reduced to  $P_{const} = 10^{-8}$ . This assumption, also considered in ARAIM [2], may be accomplished using the guidelines in [34]. These guidelines exploit additional information from the Air Navigation Service Provider (ANSP) ground segment. In Fig. 12 and 13, availability maps assume nominal 24-satellite GPS and Galileo constellations. The same color code as in Fig. 10 and 11 is used. Again, batch ARAIM in Fig. 13 provides a dramatic improvement as compared to snapshot ARAIM in Fig. 12.

Worldwide coverage of 99.5% availability, and of 95% availability (given in parentheses), for the above configurations, for both nominal and depleted constellations, are listed in Table 2. Table 2 quantifies the global performance improvement brought by batch ARAIM as compared to snapshot ARAIM. As mentioned throughout the paper, this improvement comes at the cost of higher computation and memory loads. It must also be noted that, for aircraft navigation standards that are more stringent than LPV200, and that include  $\ell = 10$  m, additional requirements are typically involved, e.g., on the communication link between ANSP ground segment and aircraft. Such considerations are beyond the scope of this paper.

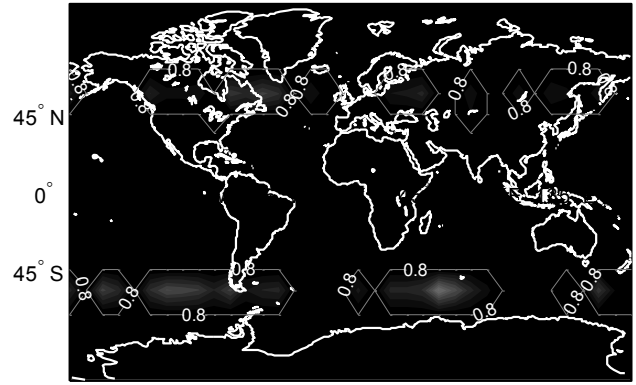


**Fig. 12 Availability Map for Snapshot ARAIM using nominal constellations,  $P_{const} = 10^{-8}$ ,  $\ell = 10$  m (coverage of 99.5% availability is 0%).**

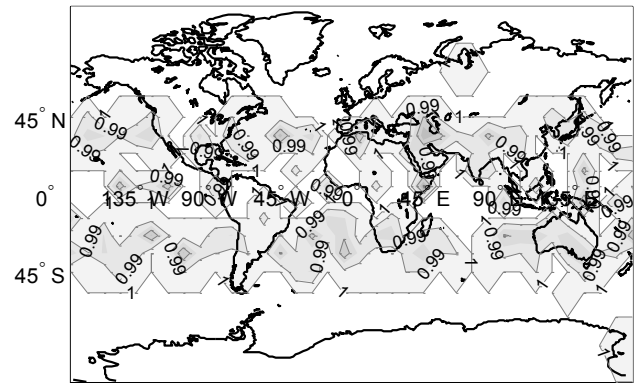


**Fig. 13 Availability Map for Batch ARAIM using nominal constellations,  $P_{const} = 10^{-8}$ ,  $\ell = 10$  m (coverage of 99.5% availability is 80%).**

**Table 2. Coverage of 99.5% Availability and Coverage of 95% Availability (in parentheses)**

	Snapshot ARAIM	Batch ARAIM
nominal constellations, $P_{const} = 10^{-4}$ , $\ell = 35$ m	95.6% (100%)	100% (100%)
depleted constellations, $P_{const} = 10^{-4}$ , $\ell = 35$ m	61% (99.4%)	99.6% (100%)
nominal constellations, $P_{const} = 10^{-8}$ , $\ell = 10$ m	0% (0%)	80% (99.8%)
depleted constellations, $P_{const} = 10^{-8}$ , $\ell = 10$ m	0% (0%)	29% (61%)

While Table 2 suggests that a 10 meter alert limit may be reachable using nominal constellations, additional research is needed to demonstrate whether more stringent precision approach requirements can be fulfilled.

## CONCLUSION

In this paper, a new ARAIM integrity monitoring method was devised, which exploits the motion of satellites from multiple GNSS. Raw measurement error models over time were established, which were shown to be consistent with ‘snapshot’ ARAIM assumptions on carrier-smoothed code measurements in [1, 2]. These raw measurements were then incorporated in batch-type estimation and solution-separation fault-detection processes.

The impact of satellite motion on ‘batch ARAIM’ was analyzed as a functions of batch period, and then quantified globally in comparison with conventional ‘snapshot ARAIM’. The proposed batch ARAIM implementation is slightly more computation and memory expensive than snapshot ARAIM. But, it can provide dramatic performance improvements both when aiming to achieve LPV200 requirements using depleted constellations, and when trying to meet a much more stringent 10 meter alert limit.

The next step of this research is to validate the raw measurement error models over time using large amounts of experimental data.

## ACKNOWLEDGMENTS

The authors would like to thank the Federal Aviation Administration (FAA) for their support of this research. However, the opinions in this paper are our own and do not necessarily represent those of any other person or organization.

## APPENDIX: MEASUREMENT ERROR CORRELATION IN REDUCED BATCH IMPLEMENTATION

This appendix provides analytical expressions of the correlation between CSC and raw carrier measurements. These expressions are needed to express the measurement noise covariance matrix  $\bar{\mathbf{V}}$  of vector  $[\mathbf{v}_{RNM,\rho}^T \quad \mathbf{v}_{RNM,\bar{\rho}}^T]$  in equation (26).

Equations are provided assuming time-correlated raw code and carrier phase noise modeled as first order Gauss-Markov processes with a time constant  $T_{MP}$ :

$$\varepsilon_{\rho,k} = \beta \varepsilon_{\rho,k-1} + v_{\rho,k} \quad (\text{A.1})$$

$$\varepsilon_{\phi,k} = \beta \varepsilon_{\phi,k-1} + v_{\phi,k} \quad (\text{A.2})$$

where  $v_{\rho,k}$  and  $v_{\phi,k}$  are white random sequences, and:

$$\beta = e^{-T_s/T_{MP}} \quad (\text{A.3})$$

These models are used to account for multipath (assuming  $T_{MP}=80\text{s}$ ) and receiver noise (assuming  $\beta=0$ ).

We can express the raw carrier phase measurement time correlation as:

$$E\{\varepsilon_{\phi,k-1}\varepsilon_{\phi,k}\} = E\{\varepsilon_{\phi,k-1}(\beta\varepsilon_{\phi,k-1} + v_{\phi,k})\} = \beta\sigma_{\phi,k-1}^2 \quad (\text{A.4})$$

where  $E\{\}$  is the expected value operator, and where we defined  $\sigma_{\phi,k}^2 \equiv E\{\varepsilon_{\phi,k}\varepsilon_{\phi,k}\}$ . For the reduced batch implementation, measurements are taken at infrequent time intervals, much larger than the raw data sampling period. Let us define the number  $K$  of raw samples in-between two successive reduced-batch samples.  $K$  is given by:

$$K = T_{RBS}/T_s \quad (\text{A.5})$$

For example, for values used in performance analysis,  $K=600$ . Over  $T_{RBS}$ , equation (A.4) becomes:

$$E\{\varepsilon_{\phi,k-K}\varepsilon_{\phi,k}\} = \beta^K \sigma_{\phi,k-K}^2 \quad (\text{A.6})$$

For  $K=600$ ,  $T_s=0.5\text{s}$  and  $T_{MP}=80\text{s}$ , we can use the following approximation:  $E\{\varepsilon_{\phi,k-K}\varepsilon_{\phi,k}\} \approx 0$ .

In addition, the HF CSC measurement equation is expressed as:

$$\varepsilon_{\bar{\rho},k} = \frac{1}{\alpha} \varepsilon_{\rho,k} + \frac{\alpha-1}{\alpha} (\varepsilon_{\bar{\rho},k-1} + \varepsilon_{\phi,k} - \varepsilon_{\phi,k-1}) \quad (\text{A.7})$$

where  $\alpha = T_{HF}/T_s$  (A.8)

Equation (A.7) is used to evaluate the correlation between  $\varepsilon_{\bar{\rho},k}$  and  $\varepsilon_{\phi,k}$ , which can be written as:

$$\begin{aligned} & E\{\varepsilon_{\bar{\rho},k}\varepsilon_{\phi,k}\} \\ &= E\left\{\left[\frac{1}{\alpha}\varepsilon_{\rho,k} + \frac{\alpha-1}{\alpha}(\varepsilon_{\bar{\rho},k-1} + \varepsilon_{\phi,k} - \varepsilon_{\phi,k-1})\right]\varepsilon_{\phi,k}\right\} \\ &= \frac{1}{\alpha} E\{\varepsilon_{\rho,k}\varepsilon_{\phi,k}\} + \frac{\alpha-1}{\alpha} E\{\varepsilon_{\bar{\rho},k-1}\varepsilon_{\phi,k}\} \\ &\quad + \frac{\alpha-1}{\alpha} E\{\varepsilon_{\phi,k}\varepsilon_{\phi,k}\} - \frac{\alpha-1}{\alpha} E\{\varepsilon_{\phi,k-1}\varepsilon_{\phi,k}\} \\ &= 0 + \frac{\alpha-1}{\alpha} \beta E\{\varepsilon_{\bar{\rho},k-1}\varepsilon_{\phi,k-1}\} + \frac{\alpha-1}{\alpha} \sigma_{\phi,k}^2 - \frac{\alpha-1}{\alpha} \beta \sigma_{\phi,k-1}^2 \end{aligned}$$

Assuming that  $E\{\varepsilon_{\bar{\rho},k}\varepsilon_{\phi,k}\} \approx E\{\varepsilon_{\bar{\rho},k-1}\varepsilon_{\phi,k-1}\}$ , which is realistic because measurement noise correlation characteristics do not change over one time step of  $T_S = 0.5$  s, we obtain the following expression:

$$E\{\varepsilon_{\bar{\rho},k}\varepsilon_{\phi,k}\} = \frac{\alpha-1}{\alpha+(1-\alpha)\beta}(\sigma_{\phi,k}^2 - \beta\sigma_{\phi,k-1}^2) \quad (\text{A.9})$$

The carrier phase measurement variance  $\sigma_{\phi,k}^2$  changes over time: it is elevation-dependent and varies with satellite motion. But it is constant over  $T_S = 0.5$  s, so that equation (A.9) becomes:

$$E\{\varepsilon_{\bar{\rho},k}\varepsilon_{\phi,k}\} = \gamma(\alpha-1)(1-\beta)\sigma_{\phi,k}^2 \quad (\text{A.10})$$

where 
$$\gamma = \frac{1}{\alpha+(1-\alpha)\beta} \quad (\text{A.11})$$

The same assumptions, and the same type of derivations are used to establish the following results, which are needed to populate  $\bar{\mathbf{V}}$ :

$$E\{\varepsilon_{\bar{\rho},k-K}\varepsilon_{\phi,k}\} = \gamma(\alpha-1)(1-\beta)\beta^K\sigma_{\phi,k-K}^2 \quad (\text{A.12})$$

$$E\{\varepsilon_{\bar{\rho},k}\varepsilon_{\phi,k-K}\} = \gamma(\alpha-1)(\beta-1)\beta^{K-1}\sigma_{\phi,k-K}^2 \quad (\text{A.13})$$

One of the most challenging terms to obtain is the time-correlation of CSC measurements over time. Time-correlation is caused both by multipath and by the HF, which keeps a finite memory of past measurements. A full derivation is not provided here to limit the length of the paper, but the following result was obtained:

$$\begin{aligned} & E\{\varepsilon_{\bar{\rho},k}\varepsilon_{\bar{\rho},k-K}\} \\ &= \zeta_K \left( \frac{1}{\alpha}\beta\gamma\sigma_{\rho,k-K}^2 - \frac{(\alpha-1)^2}{\alpha}(\beta-1)^2\gamma\sigma_{\phi,k-K}^2 \right) \\ & \quad + \left( \frac{\alpha-1}{\alpha} \right)^K \sigma_{\bar{\rho},k-K}^2 \end{aligned} \quad (\text{A.14})$$

where we used the notations:

$$\zeta_K = \sum_{i=0}^{K-1} \left( \frac{\alpha-1}{\alpha} \right)^{K-1-i} \beta^i \quad (\text{A.15})$$

$$\sigma_{\bar{\rho},k}^2 \equiv E\{\varepsilon_{\bar{\rho},k}\varepsilon_{\bar{\rho},k}\}, \quad \sigma_{\rho,k}^2 \equiv E\{\varepsilon_{\rho,k}\varepsilon_{\rho,k}\} \quad (\text{A.16})$$

It is worth noting that when  $T_{RBS} \gg T_{MP}$ , and  $T_{RBS} \gg T_{HF}$ , which is the case in our performance analysis, the correlation terms in equations (A.6) and (A.12) to (A.14)

cancel to zero. The only non-zero terms left in  $\bar{\mathbf{V}}$  are the known quantities  $\sigma_{\phi,k}^2 \equiv E\{\varepsilon_{\phi,k}\varepsilon_{\phi,k}\}$ ,  $\sigma_{\bar{\rho},k}^2 \equiv E\{\varepsilon_{\bar{\rho},k}\varepsilon_{\bar{\rho},k}\}$ , and  $E\{\varepsilon_{\bar{\rho},k}\varepsilon_{\phi,k}\}$  in equation (A.10).

## REFERENCES

- [1] Working Group C. "ARAIM Technical Subgroup. Interim Report Issue 1.0." Technical report, EU-US Cooperation on Satellite Navigation, 2012.
- [2] Working Group C. "ARAIM Technical Subgroup. Milestone 2.0 Report." Technical report, EU-US Cooperation on Satellite Navigation, 2014.
- [3] Blanch, J., T. Walter, P. Enge, S. Wallner, F. A. Fernandez, R. Dellago, R. Ioannides, I. F. Hernandez, B. Belabbas, A. Spletter, M. Rippl, "Critical Elements for a Multi-Constellation Advanced RAIM," *NAVIGATION*, Vol. 60, No. 1, 2013, pp. 53-69.
- [4] Remondi, B., "Pseudo-Kinematic GPS Results Using the Ambiguity Function Method," *Proceedings of the 46th Annual Meeting of the Institute of Navigation*. Atlantic City, NJ. 41-49, NJ, 1990.
- [5] Lee, Y. C., "Analysis of Range and Position Comparison Methods as a Means to Provide GPS Integrity in the User Receiver," *Proc. of the 42nd Annual Meeting of The Institute of Navigation*, Seattle, WA, 1986, pp. 1-4.
- [6] Parkinson, B. W., and Axelrad, P., "Autonomous GPS Integrity Monitoring Using the Pseudorange Residual," *NAVIGATION*, Vol. 35, No. 2, 1988, pp. 225-274.
- [7] Blanch, J., Walter, T., and Enge, P., "Optimal Positioning for Advanced RAIM," *NAVIGATION, Journal of The Institute of Navigation*, Vol. 60, No. 4, 2013, pp. 279-289.
- [8] Blanch, J., Walter, T., Enge, P., "Results on the Optimal Detection Statistic for Integrity Monitoring," *Proceedings of the 2013 International Technical Meeting of The Institute of Navigation*, San Diego, California, January 2013, pp. 262-273.
- [9] Joerger, M., Langel, S., and Pervan, B., "Integrity Risk Minimization in RAIM - Part 2 - Optimal Estimator Design," submitted to *Journal of Navigation of the Royal Institute of Navigation*, 2014.
- [10] Joerger, M., Langel, S., and Pervan, B., "Integrity Risk Minimization in RAIM - Part 1 - Optimal Detector Design." submitted to *Journal of Navigation of the Royal Institute of Navigation*, 2014.
- [11] Radio Technical Commission for Aeronautics (RTCA) Special Committee 159. "Minimum Aviation System Performance Standards for the Local Area Augmentation System (LAAS)." Document RTCA/DO-245, 2004.

- [12] Crassidis, J., and Junkins, J., *Optimal Estimation of Dynamic Systems*, Chapman & Hall/CRC, Boca Raton, FL, 2004, pp. 123-174.
- [13] Joerger, M., Gratton, L., Pervan, B., and Cohen, C. E., "Analysis of Iridium-Augmented GPS for Floating Carrier Phase Positioning," *NAVIGATION, Journal of The Institute of Navigation*, Vol. 57, No. 2, 2010, pp. 137-160.
- [14] Brenner, M., "Integrated GPS/Inertial Fault Detection Availability," *Proceedings of the 8th International Technical Meeting of the Satellite Division of The Institute of Navigation (ION GPS 1995)*, Palm Springs, CA, 1995, pp. 1949-1958.
- [15] Pervan, B., "Navigation Integrity for Aircraft Precision Landing Using the Global Positioning System," PhD Thesis, Stanford University, Stanford, CA, 1996.
- [16] Cohen, C., Cobb, S., Lawrence, D., Pervan, B., Powell, D., Parkinson, B., Aubrey, G., Loewe, W., Ormiston, D., McNally, D., Kaufmann, D., Wullschlegel, V., and Swider, R., "Autoland a 737 Using GPS Integrity Beacons," *NAVIGATION: Journal of the Institute of Navigation*, Vol 42, No. 3, 1995, pp. 467-486.
- [17] Gutt, G., Fischer, S., Sheen, J., and Lawrence, D., "Precision Autoland Guidance of the X-31 Aircraft Using IBL - The Integrity Beacon Landing System," *AIAA Guidance, Navigation, and Control Conference*, Providence, RI, 2004.
- [18] Rabinowitz, M., Parkinson, B., Cohen, C., O'Connor, M., Lawrence, D., "A System Using LEO Telecommunication Satellites for Rapid Acquisition of Integer Cycle Ambiguities," *Proceedings of ION/IEEE Position Location and Navigation Symposium*, Palm Springs, CA, 1998, pp. 137-145.
- [19] Murphy, T., Harris, M., Geren, P., Pankaskie, T., Clark, B., and Burns, J., "More Results from the Investigation of Airborne Multipath Errors," *Proceedings of the 18th International Technical Meeting of the Satellite Division of The Institute of Navigation (ION GNSS 2005)*, Long Beach, CA, September 2005, pp. 2670-2687.
- [20] Murphy, T., Harris, M., Beauchamp, S., "Implications of 30-Second Smoothing for GBAS Approach Service Type D," *Proceedings of the 2010 International Technical Meeting of The Institute of Navigation*, San Diego, CA, January 2010, pp. 376-385.
- [21] McGraw, G., Murphy, T., Brenner, M., Pullen, S., and Van Dierendonck, A., "Development of the LAAS Accuracy Models," *Proceedings of the Institute of Navigation GPS Conference*. Salt Lake City, UT, 2000, pp. 1212-1223.
- [22] Parkinson, B., and Spilker, J., 1996, *Global Positioning System: Theory and Applications Volume 1*, AIAA Progress in Aeronautics and Astronautics, Washington, DC, Volume 163.
- [23] Warren, D., Raquet, J., "Broadcast vs. Precise GPS Ephemerides: a Historical Perspective," *GPS Solutions*, Vol. 7, 2003, pp. 151-156.
- [24] Gratton, L., "Orbit Ephemeris Monitors for Category I Local Area Augmentation of GPS," MS Thesis, Illinois Institute of Technology, Chicago, IL, 2003.
- [25] Cohenour, C., and van Graas, F., "GPS Orbit and Clock Error Distributions," *NAVIGATION, Journal of The Institute of Navigation*, Vol. 58, No. 1, Spring 2011, pp. 17-28.
- [26] DeCleene, B., "Defining Pseudorange Integrity - Overbounding," *Proceedings of the 13th International Technical Meeting of the Satellite Division of The Institute of Navigation (ION GPS 2000)*, Salt Lake City, UT, September 2000, pp. 1916-1924.
- [27] Rife, J. Pullen, S., Enge, P., and Pervan, B., "Paired Overbounding for Nonideal LAAS and WAAS Error Distributions," *IEEE Transactions on Aerospace and Electronic Systems*, Vol. 42, No. 4, 2006, pp. 1386-1395.
- [28] Chan, F-C., Joerger, M., Pervan, B., "High Integrity Stochastic Modeling of GPS Receiver Clock for Improved Positioning and Fault Detection Performance," *Proceedings of IEEE/ION PLANS 2010*, Indian Wells, CA, May 2010, pp. 1245-1257.
- [29] Joerger, M., "Carrier Phase GPS Augmentation Using Laser Scanners and Using Low Earth Orbiting Satellites." Ph.D. Dissertation, Illinois Institute of Technology, 2009.
- [30] Joerger, M., Chan, F.-C., Pervan, B., "Solution Separation Versus Residual-Based RAIM", *NAVIGATION, Journal of The Institute of Navigation*, Vol. 61, No. 4, Winter 2014, pp. 273-291.
- [31] Blanch, J., Ene, A., Walter, T., and Enge, P., "An Optimized Multiple Hypothesis RAIM Algorithm for Vertical Guidance," *Proceedings of the 20th International Technical Meeting of the Satellite Division of The Institute of Navigation (ION GNSS 2007)*, Fort Worth, TX, September 2007, pp. 2924-2933.
- [32] Chan, F-C., Pervan, B., "A Practical Approach to RAIM-based Fault-Tolerant Position Estimation," *Proceedings of the 23rd International Technical Meeting of the Satellite Division of The Institute of Navigation (ION GNSS 2010)*, Portland, OR, September 2010, pp. 3181-3190.
- [33] almanac files provided by Stanford University, available online at <http://waas.stanford.edu/staff/maast/maast.html>
- [34] Walter, T., Blanch, J., "Airborne Mitigation of Constellation Wide Faults," *Proceedings of the 2015*

*International Technical Meeting of The Institute of Navigation*, Dana Point, California, January 2015, pp. 676-686.